First Evidence of Intrinsic Alignments of Red Galaxies at $z > 1$: Cross Correlation between CFHTLenS and FastSound Samples

Motonari Tonegawa[1] and Teppei Okumura[2,3]
[1] Asia Pacific Center for Theoretical Physics, Pohang, 37673, Republic of Korea
[2] Institute of Astronomy and Astrophysics, Academia Sinica, No. 1, Section 4, Roosevelt Road, Taipei 10617, Taiwan
[3] Kavli Institute for the Physics and Mathematics of the Universe (WPI), UTIAS, The University of Tokyo, Kashiwa, Chiba 277-8583, Japan
Received 2021 September 29; revised 2021 December 8; accepted 2021 December 10; published 2021 December 31

Abstract

We report the first evidence for intrinsic alignment (IA) of red galaxies at $z > 1$. We measure the gravitational shear-intrinsic ellipticity cross correlation function at $z \sim 1.3$ using galaxy positions from the FastSound spectroscopic survey and galaxy shapes from the Canada France Hawaii telescope lensing survey data. Adopting the nonlinear alignment model, we obtain a 2.4σ level detection of the IA amplitude $A^{\mathrm{LA}} = 27.48^{+11.53}_{-11.54}$ (and 2.6σ with $A^{\mathrm{LA}} = 29.43^{+11.48}_{-11.49}$ when weak lensing contaminations are taken into account), which is larger than the value extrapolated from the constraints obtained at lower redshifts. Our measured IA is translated into a $\sim 20\%$ contamination of the weak-lensing power spectrum for the red galaxies. This marginal detection of IA for red galaxies at $z > 1$ motivates the continuing investigation of the nature of IA for weak lensing studies. Furthermore, our result provides the first step to utilize IA measurements in future high-z surveys as a cosmological probe, complementary to galaxy clustering and lensing.

Unified Astronomy Thesaurus concepts: Large-scale structure of the universe (902); Gravitational lensing (670)

1. Introduction

Intrinsic alignment (IA) is a coherent alignment of galaxy orientations with the surrounding large-scale structure caused by the local gravitational interaction (Croft & Metzler 2000; Heavens et al. 2000; Catelan et al. 2001; Hirata & Seljak 2004). IA has been considered one of the main contaminants of weak lensing surveys, where the source galaxies are assumed to be randomly oriented. While weak lensing is a major probe to constrain cosmological parameters, it requires an accurate modeling of IA to avoid constraints being biased (Joachimi et al. 2015), and thus we need to understand how large the IA effect is and how it depends on scales and time. IA also contains useful information about galaxy formation and evolution. Galaxies at higher redshifts could be either more strongly or weakly aligned because of shorter time elapsing for internal and external interactions, e.g., structure formations and mergers, to boost or suppress IAs. Therefore, measuring the IA at various redshifts will help constrain dynamical aspects of galaxy evolution models.

Furthermore, due to the fact that galaxy shapes are linearly related to the gravitational potential on cosmological scales, there is a growing interest in using IA as a new tool to constrain cosmological models (Chisari & Dvorkin 2013; Taruya & Okumura 2020). Since ongoing and future deep surveys provide high-quality galaxy images toward high redshifts, IA can be a powerful cosmological probe complementary to galaxy clustering and weak lensing.

The IA of elliptical galaxies has been observed at $z < 1$ by measuring intrinsic ellipticity correlations and has been shown to contaminate the weak-lensing power spectrum by $\sim 10\%$ (Mandelbaum et al. 2006; Hirata et al. 2007;

Okumura & Jing 2009; Okumura et al. 2009; Singh et al. 2015; Johnston et al. 2021). Extending such observations to higher redshifts is important to better understand IA as a cosmological probe and as a source of contamination in weak lensing studies.

Motivated by these findings, in this paper, we report the first possible evidence for IA of red galaxies at $z > 1$ by cross correlating the shape sample selected from the Canada France Hawaii Telescope Lensing Survey (CFHTLenS; Erben et al. 2013) data with the galaxy density sample from the Subaru FastSound survey (Tonegawa et al. 2015).

The cosmological parameters used in this paper are $(\Omega_m, \Omega_\Lambda, h, \sigma_8) = (0.3, 0.7, 0.7, 0.8)$, except when we use $h = 1.0$ to calculate the absolute luminosity for consistency with preceding studies. All the distances and separations are expressed in comoving units.

2. Data

2.1. CFHTLenS Shape Sample

Current spectroscopic samples of elliptical galaxies for high redshifts are not sufficiently large because one needs a long exposure time to observe the 4000 Å breaks. We thus use the publicly available CFHTLenS (Erben et al. 2013) data for the shape sample.[4] It provides accurate photometric redshifts (photo-z; Hildebrandt et al. 2012) and shape measurements for galaxies covering $154 \deg^2$ over the CFHT Wide fields. The typical photo-z scatter is $\sigma_z/(1 + z) \sim 0.04$ at $z > 1$. We take the data in the photo-z range, $1.13 < z_{\mathrm{ph}} < 1.63$, which covers the entire redshift range of the spectroscopic FastSound sample described below. We also limit the data to the angular regions overlapping with the FastSound sky coverage, explained in the following subsection. We exclude stars from our sample, which are assigned zero ellipticity. Galaxies in the catalog are classified by spectral type,

---

[4] http://www.cadc-ccda.hia-iha.nrc-cnrc.gc.ca/en/community/CFHTLens/query.html

symbolized as a numeric flag T_B,[5] estimated by the Bayesian photometric redshift code (Benítez 2000) using the template set of Capak (2004). Smaller (larger) T_B values correspond to redder (bluer) galaxies, and we adopt T_B < 1.5 to select elliptical galaxies which are expected to have strong IA signals. The criterion results in 11,320 galaxies, 12% of all the galaxies in the redshift range.

The two-component ellipticity of galaxies is given by $(e_+, e_\times) = \frac{1-q}{1+q}(\cos 2\phi, \sin 2\phi)$, where q is the minor-to-major-axis ratio on the celestial sphere and ϕ is the position angle. The ellipticity is estimated using *lensfit* (Miller et al. 2007) applied to the i'-band image and corrected for the additive and the multiplicative biases as done in Tonegawa et al. (2018).

2.2. FastSound Spectroscopic Sample

FastSound is a spectroscopic survey with the FMOS instrument (Iwamuro et al. 2012) to measure redshifts of $\sim$4000 blue star-forming galaxies at $z \sim 1.36$ (Tonegawa et al. 2015; Okada et al. 2016) in $\sim$25 deg^2 of the CFHT Wide fields. Out of the four regions of the CFHT Wide, we use the W2 and W3 fields because these fields cover the majority of FastSound. As the survey used near-infrared spectroscopy targeting Hα6563, the galaxy sample ranges from $z = 1.19$ to 1.55. We select galaxies that have emission-line features with signal-to-noise ratio (S/N) greater than 4.5, obtaining 2665 objects. To measure correlation functions we use the random catalog constructed in Okumura et al. (2016).

3. Galaxy-intrinsic Ellipticity Correlation Function

This study focuses on the galaxy-intrinsic ellipticity (GI) correlation, with the density field from the FastSound galaxy sample and the ellipticity field from the CFHTLenS photo-z galaxy sample. We do not consider the auto-correlation of the intrinsic ellipticity (II) because it is noisier than the GI correlation and more severely affected by the photo-z uncertainties in our analysis.

We propose an estimator for the GI cross correlation function, which is an extension of the Hamilton estimator of the galaxy cross correlation function (Hamilton 1993; Wang et al. 2011):

$$\xi_{g+}(\bar{r}_p, \bar{r}_\pi) = \frac{S^+Q \cdot RR - S^+R \cdot QR}{QR \cdot DR}, \qquad (1)$$

where $(\bar{r}_p, \bar{r}_\pi)$ are the transverse and parallel separations of galaxy pairs, respectively. The term RR is the pair count of the random sample, QR (DR) is the cross pair count between spectroscopic (photometric) and random samples, and S^+Q (S^+R) denotes the sum of the tangential shear component, e_+, redefined relative to the direction to the spectroscopic (random) sample. To account for the uncertainty of shape measurements, e_+ is weighted by the inverse variance. We put a bar on the separations to explicitly denote that they are affected by photo-z (see Section 4.2 for their relation to spectroscopically determined (r_p, r_π)).

We integrate the 3D GI correlation function along the line of sight to minimize the effect of both photo-z errors and redshift-space distortions,

$$w_{g+}(\bar{r}_p) = \int_{-\bar{r}_{\pi,\max}}^{\bar{r}_{\pi,\max}} \xi_{g+}(\bar{r}_p, \bar{r}_\pi) d\bar{r}_\pi, \qquad (2)$$

where the value of $\bar{r}_{\pi,\max}$ needs to be chosen to include the correlated pairs scattered by the photo-z errors[6] while minimizing large-scale noise. We carefully tested the integral range and found that $\bar{r}_{\pi,\max} = 160 \, h^{-1}$ Mpc with the linear bin width $\Delta \bar{r}_\pi = 5 \, h^{-1}$ Mpc provides the highest S/N. We will discuss the choice of $\bar{r}_{\pi,\max}$ more in Section 4. We also measured $w_{g\times}$ by replacing e_+ with $e_\times$ and use it for systematic tests because this quantity should be zero at all scales. We have also tried another estimator for the correlation function (Mandelbaum et al. 2006; Joachimi et al. 2011),

$$\xi_{g+}(\bar{r}_p, \bar{r}_\pi) = \frac{S^+Q - S^+R}{DR}. \qquad (3)$$

We have confirmed that the two estimators gave the same results (see Appendix A).

The covariance matrix for the GI correlation function is estimated using 82 jackknifed realizations as done in Tonegawa et al. (2018). The survey regions were split into 33 (49) subregions for W2 (W3), each with a side length of $\sim$25 h^{-1} Mpc. The covariance matrix is estimated for each of the W2 and W3 realizations and they are combined following the inverse-variance weighting (see, e.g., Okumura et al. 2021).

In the FastSound survey, some targets are not assigned fibers due to their finite number and this affects the correlation function measurement at an angular scale of $\sim$1′ (Okumura et al. 2016). However, this effect is significantly alleviated by considering the cross correlation with a photo-z sample.

### 4. Results and Discussions

4.1. The GI Correlation Functions

We show the GI cross correlation function between the FastSound galaxy positions and CFHT red galaxy shapes, w_{g+}, as the solid red line in the upper panel of Figure 1. We take nine logarithmic bins from $\bar{r}_p = 1$ to $100 \, h^{-1}$ Mpc. The error bars represent $1 - \sigma$ uncertainties estimated from the 82 jackknifed realizations. We see a small but nonzero signal in the w_{g+} measurement. The positive correlation means that the major axes of CFHT red galaxies tend to point toward overdensities. The bottom panel of Figure 1 shows the other GI cross correlation function, $w_{g\times}$, which should vanish on all scales. The signal of $w_{g\times}$ is consistent with zero beyond $3 \, h^{-1}$ Mpc. We perform a further test by shuffling the ellipticity information in the shape sample before measuring the GI correlation and find that the resulting correlation is indeed consistent with zero beyond the scale, as shown in Appendix A. We thus consider our measurements free from observational systematics at $\bar{r}_p > 3 \, h^{-1}$ Mpc and use this scale for the following analysis.

To see the detection significance for the IA signal, we fit a power-law model, $w_{g+}^{\mathrm{PL}}(\bar{r}_p) = (1 - f_{\mathrm{blund}})A^{\mathrm{PL}}\left(\frac{\bar{r}_p}{20 \, h^{-1} \, \mathrm{Mpc}}\right)^\gamma$, to the measured correlation function. The parameter f_{blund} is a fraction of

---

[5] For the correspondence between T_B and galaxy types, see Erben et al. (2013).

[6] This effect elongates the correlation function along the line of sight, similarly to the small-scale redshift-space distortion, where virialized galaxy motions cause random displacements of observed galaxy positions (Hamilton 1998).
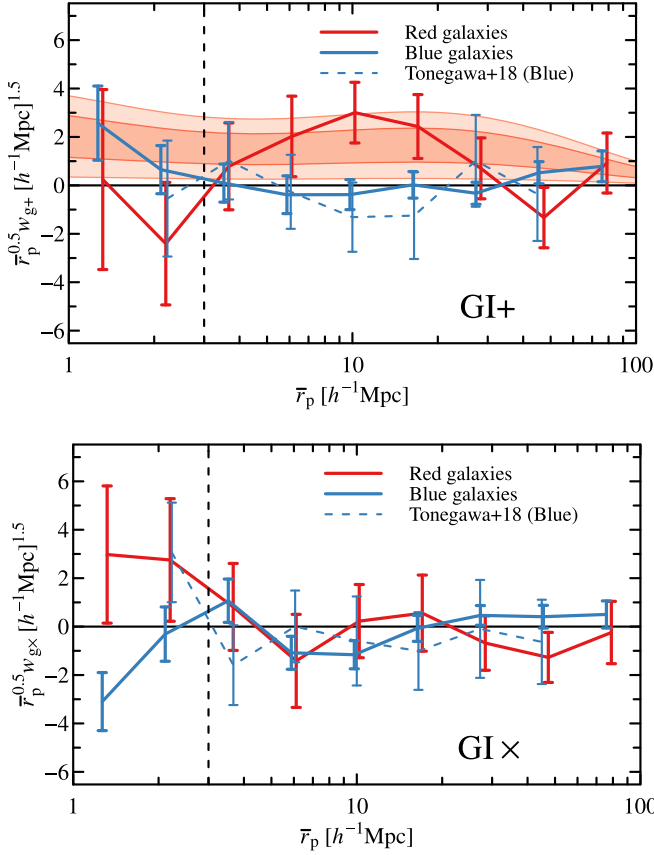
Figure 1. Projected correlation functions, w_{g+} (top) and $w_{g\times}$ (bottom) as a function of transverse separation $\bar{r}_p$. We use the FastSound sample for the galaxy density field for all the measurements presented here. We use the different shape samples as the galaxy shape field for different lines: red galaxies (red lines) and blue galaxies (blue solid lines). The blue dashed line is the GI correlation of the FastSound blue galaxies measured by Tonegawa et al. (2018). The dark and light red shaded regions in the top panel indicate the 68% and 95% confidence intervals of the best-fitting NLA model obtained for red galaxies at $\bar{r}_p > 3\,h^{-1}$ Mpc denoted by the vertical lines. The error bars are obtained from the diagonal elements of the covariance matrix, $C_{\mathrm{ii}}^{1/2}$.

redshift blunders (noise lines and O_{III} doulets) and $f_{\mathrm{blund}} = 0.071$ for our FastSound sample (Okada et al. 2016; Okumura et al. 2016). Taking account of the full covariance matrix, we calculate χ^2 statistics in the range of $3 < \bar{r}_p < 100\,h^{-1}$ Mpc, where $w_{g\times}$ is consistent with zero. We fix $\gamma = -0.88$, as obtained by Hirata et al. (2007) for luminous red galaxies (LRGs) at $z \simeq 0.3$. This is a reasonable assumption because we obtain $\gamma = -0.75^{+0.42}_{-0.42}$ when we simultaneously determine A^{PL} and γ. The resulting constraint on the amplitude parameter is $A^{\mathrm{PL}} = 0.266^{+0.112}_{-0.116}$ (68% CL), corresponding to a 2.3σ detection of IA.

Our finding is robust because a cross correlation function tends to be uncorrelated between two independent samples and thus less sensitive to systematic effects. Furthermore, we have varied several parameters to confirm that the signal is still detectable. Specifically, we have applied $\bar{r}_{\pi,\mathrm{max}} = 200\,h^{-1}$ Mpc and confirmed the signal at $\sim 2\sigma$. Also, changing the T_B threshold to 1.1 (selecting a redder population) resulted in a similar detection significance. Therefore, we conclude that the signal indeed indicates evidence of IA.

Unlike red galaxies, we do not find nonzero GI correlations for the CFHT blue galaxy shapes, selected by the criteria of $2.0 < $ T_B < 4.0, as seen as the solid blue line in Figure 1. This

is consistent with the result of Tonegawa et al. (2018), as shown as the blue dashed line for comparison, who measured the GI auto-correlations of blue galaxies that are spectro-scopically confirmed from the FastSound at $z \sim 1.36$. Other studies at lower redshifts also have not found any GI signal for blue galaxies (Mandelbaum et al. 2011; Johnston et al. 2021). IA of spiral galaxies are likely to be explained by the quadratic alignment model (Catelan et al. 2001; Hirata & Seljak 2004, 2010; Kirk et al. 2015), and the model indeed predicts null GI signals for a Gaussian density field.

4.2. Linear Alignment Model

Here we consider a more physically motivated prediction of IA, the linear alignment (LA) model (Catelan et al. 2001; Hirata & Seljak 2004) which relates the shear field linearly to the gravitational potential. Under this model the density-intrinsic ellipticity power spectrum at redshift z is given by

$$P_{\delta I}(k, z) = \frac{C_1 \bar{\rho}(z)}{(1+z)D(z)} a^2 P_\delta(k, z), \qquad (4)$$

where $\bar{\rho}(z)$ is the mean matter density, $D(z)$ is the growth factor, and $P_\delta(k, z)$ is the matter power spectrum. While the original LA model used linear theory prediction for P_δ (Hirata & Seljak 2004), using the nonlinear matter power spectrum was found to better explain the observed IA (nonlinear LA, NLA; Bridle & King 2007; Blazek et al. 2011). Therefore, we use the nonlinear matter spectrum of Takahashi et al. (2012) to obtain the theoretical prediction. The normalization parameter C_1 varies much with given galaxy samples. Following the convention, we introduce another parameter, A^{LA}, as $A^{\mathrm{LA}} = C_1 \rho_{\mathrm{cr}}/0.0134$, where ρ_{cr} is the critical density.

The Hankel transform converts the power spectrum into the 3D gI correlation function (Okumura & Taruya 2020; Okumura et al. 2020):

$$\xi_{\mathrm{gI}}^{\mathrm{spec}}(r_p, r_\pi, z) = (1 - \mu^2) b_g \int_0^\infty \frac{k^2 dk}{2\pi^2} P_{\delta I}(k, z) j_2(kr), \quad (5)$$

where $\mu = r_\pi/r$ with $r = \sqrt{r_p^2 + r_\pi^2}$, j_2 is the spherical Bessel function of the second order, and b_g is the linear bias parameter of the FastSound galaxies, $b_g = 1.9$ (Okumura et al. 2016). We use photo-z for the shape sample, which modulates Equation (5) due to the scatter along the line of sight as (Joachimi et al. 2011; see also Appendix B.1)

$$\xi_{\mathrm{gI}}(\bar{r}_p, \bar{r}_\pi, \bar{z}_{\mathrm{m}}) = \int dz_2\, p_\epsilon(z_2|\bar{z}_2)$$
$$\times \xi_{\mathrm{gI}}^{\mathrm{spec}}\left(\bar{r}_p \frac{\chi(z_{\mathrm{m}})}{\chi(\bar{z}_{\mathrm{m}})}, \frac{c\,|z_2 - z_1|}{H(z_{\mathrm{m}})}, z_{\mathrm{m}}\right), \qquad (6)$$

where $\bar{z}_{\mathrm{m}}$ denotes the mean of photo-z of the shape sample and spec-z of the density sample, a bar means a quantity affected by photo-z, H is the Hubble parameter, c is the speed of light, $\chi(z)$ is the comoving distance, $z_1 = \bar{z}_{\mathrm{m}} - \bar{r}_\pi H(\bar{z}_{\mathrm{m}})/2c$, and $p_\epsilon(z|\bar{z})$ denotes the probability distribution of the true redshift z for a given photo-z, $\bar{z}$, for the shape sample. We assume that the error in photo-z follows the normal distribution with $\sigma_z/(1 + \bar{z}) = 0.04$ (Hildebrandt et al. 2012). We integrate $\xi_{\mathrm{gI}}(\bar{r}_p, \bar{r}_\pi, \bar{z}_{\mathrm{m}})$ along the line of sight to obtain the projected correlation function $w_{g+}(\bar{r}_p)$, similarly to Equation (2). With our

Table 1
Summary of the IA Amplitude for Various Sample Redshifts and Luminosities

Data	$\langle z \rangle$	$\langle M_r \rangle$	A^{LA}	A^{LA} (HS04)	References
SDSS main, red	0.12	−19.88	$2.50^{+0.77}_{-0.73}$	$1.99^{+0.61}_{-0.58}$	Johnston et al. (2019)
GAMA $z < 0.26$, red	0.17	−20.47	$3.63^{+0.79}_{-0.79}$	$2.65^{+0.58}_{-0.58}$	Johnston et al. (2019)
BOSS LOWZ L1	0.28	−21.70	$8.5^{+0.9}_{-0.9}$	$5.2^{+0.5}_{-0.5}$	Singh et al. (2015)
BOSS LOWZ L2	0.28	−21.27	$5.0^{+1.0}_{-1.0}$	$3.1^{+0.6}_{-0.6}$	Singh et al. (2015)
BOSS LOWZ L3	0.28	−21.07	$4.7^{+1.0}_{-1.0}$	$2.9^{+0.6}_{-0.6}$	Singh et al. (2015)
BOSS LOWZ L4	0.28	−20.76	$2.2^{+0.9}_{-0.9}$	$1.3^{+0.5}_{-0.5}$	Singh et al. (2015)
GAMA $z > 0.26$, red	0.33	−21.64	$3.55^{+0.90}_{-0.82}$	$2.01^{+0.51}_{-0.46}$	Johnston et al. (2019)
MegaZ-LRG	0.54	−21.96	$4.51^{+0.64}_{-0.63}$	$1.98^{+0.28}_{-0.28}$	Joachimi et al. (2011)
CFHT and FastSound	1.31	−20.54	$27.48^{+11.53}_{-11.54}$	$5.15^{+2.16}_{-2.16}$	This work

Note. The mean absolute r-band magnitudes (with $h = 1.0$) are k- and e-corrected. The fourth column presents the amplitude of the LA model of Equation (4), whereas the fifth column presents the amplitude parameter in terms of the LA model in Hirata & Seljak (2004; HS04) to facilitate comparisons with previous works. Note that the values in these columns are proportional with the factor of $(1 + \langle z \rangle)^2$.

choice of $\bar{r}_{\pi,\mathrm{max}}$, $\bar{r}_{\pi,\mathrm{max}} = 160\ h^{-1}$ Mpc, we find the amplitude of $w_{g+}(\bar{r}_p)$ becomes 76% of that determined with spec-z, $w_{g+}^{\mathrm{spec}}(r_p)$. As shown by Joachimi et al. (2011), the r_p dependence remains almost unchanged when photo-z are considered. The LA model fitting to the measured $w_{g+}(\bar{r}_p)$ gives a constraint on the amplitude as $A^{\mathrm{LA}} = 27.48^{+11.53}_{-11.54}$, showing a 2.4σ deviation from zero similarly to the result obtained in Section 4.1. The dark and light red shaded regions in the top panel of Figure 1 indicate the 68% and 95% confidence levels of the NLA model.

The observed galaxy shape is the sum of the intrinsic shape and the weak lensing shear, and the galaxy density is the sum of the intrinsic one and the lensing magnification effect. Thus, not only the gI signal but also galaxy–galaxy lensing (gG), magnification-shear correlations (mG) and magnification-intrinsic correlations (mI) contribute to the observed galaxy-shape correlation (see Equation (B3)). Following Joachimi et al. (2011), we calculate the contributions of the gG, mG, and mI correlations, taking into account photo-z errors on the shape sample, as summarized in Appendix B.2. We obtain $\alpha_s = 2.56$ for Equation (B4) using our FastSound density sample at the z-band magnitude of ~ 23, corresponding to the magnitude limit of the sample. Including all the lensing effects, our constraint on A^{LA} becomes $A^{\mathrm{LA}} = 29.43^{+11.48}_{-11.49}$, with each contribution being 1.3% (gG), 5.8% (mG), and 0.5% (mI). Since our measurement is at a relatively high redshift, $z \sim 1.3$, the mG term becomes the dominant contamination. Since there is an uncertainty in determining the faint-end slope α_s, we quote the constraint without considering the lensing effect, $A^{\mathrm{LA}} = 27.48^{+11.53}_{-11.54}$, as our main result. This corresponds to a conservative constraint because the sign of the gG and mG terms is opposite of the gI term.

4.3. IA of Red Galaxies as a Function of Redshift

Table 1 and Figure 2 show the constraints on A^{LA} obtained from our analysis at $z \sim 1.3$ together with the previous studies at lower redshifts at $z < 1$. Since the amplitude of IA of galaxies strongly depends on the luminosity, we apply Galactic extinction (Schlegel et al. 1998) and $k + e$ corrections to the mean r-band absolute magnitude, $\langle M_r \rangle$, for a fair comparison of the IA of red galaxies at different redshifts. For the k-correction, we interpolate the templates between ellipticals (T_B = 1.0) and Sbc galaxies (T_B = 2.0) from Coleman et al. (1980) to create the spectral-energy density (SED) template of

T_B = 1.091, which represents our shape sample. For the e-correction, we use the PEGASE code (Fioc & Rocca-Volmerange 1999) to track the evolution of the r'-band magnitude of elliptical galaxies by stellar population synthesis modeling. We assume an instantaneous starburst model with the initial mass function of Scalo (1986), solar metallicity, and the galaxy age of 12 Gyr at $z = 0$. After $k + e$ corrections are made, $\langle M_r \rangle$ is modified from −18.81 to −20.54.

Joachimi et al. (2011) examined the luminosity and redshift dependences of A^{LA} using a parametric form,

$$A^{\mathrm{LA}}(L_r, z) = \alpha \left(\frac{L_r}{L_r^p} \right)^{\beta} \left(\frac{1 + z}{1 + z_0} \right)^{\eta}, \qquad (7)$$

where $z_0 = 0.3$ and the r-band pivot luminosity L_r^p is set to the value which corresponds to the absolute magnitude of $M_r = -22$. They obtained $\alpha = 5.76^{+0.60}_{-0.62}$, $\beta = 1.13^{+0.25}_{-0.20}$, and $\eta = -0.27^{+0.80}_{-0.79}$ from the measurements of elliptical galaxies up to $z \sim 0.5$. Singh et al. (2015) reached a similar result using the BOSS LOWZ data. Since the constraint on η in their study was not strong due to the limited redshift range probed, the scenario that the IA amplitude increases toward higher redshifts is still allowed, as suggested by recent simulations (Chisari et al. 2016; Samuroff et al. 2021) and observations (Yao et al. 2020). Nevertheless, our constraint on A^{LA} at $z \sim 1.3$ is marginally larger than the prediction made at lower redshifts by Joachimi et al. (2011), by $\sim 2\sigma$ level.

There are several possible explanations for this discrepancy though it is not significant given the relatively large error bars of our measurement. First, since the probed redshift is high, faint galaxies may fall below the survey limit, making the sample biased toward bright galaxies, which are known to have higher IA amplitudes (Singh et al. 2015). Second, the r'-band magnitude may not be proper to represent the shape sample of high-redshift galaxies. The r'-band magnitude is known as a good proxy of the stellar mass (Mahajan et al. 2018; Du et al. 2020), but it corresponds to $\lambda \sim 2000$–3000 Å at $z \sim 1.3$, which is below the 4000 Å break. We only expect weak SED, regardless of the actual stellar mass, and hence r'-band magnitudes may not represent the stellar and total mass. The k-correction accounts for the wavelength dependence, but it will suffer from a large uncertainty due to the uncertainty of the depth of the SED breaks. For a consistent comparison of the IA strength over a wide redshift range, other physical quantities
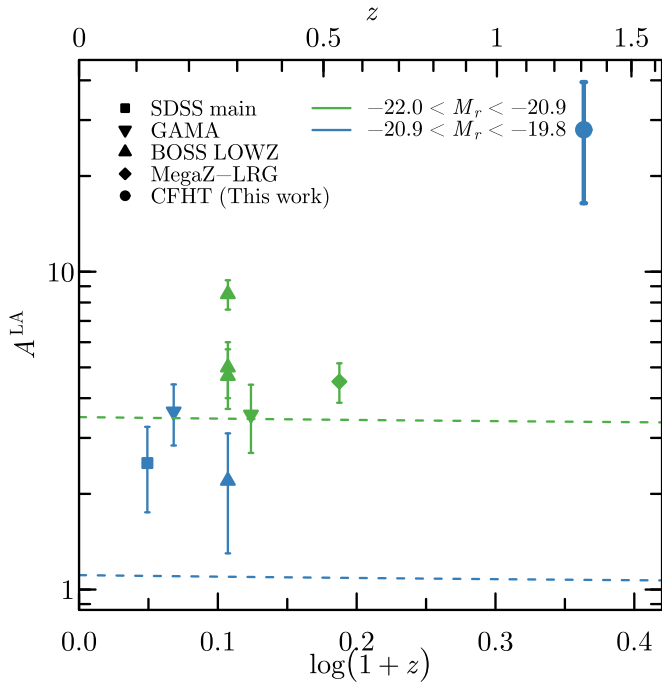
Figure 2. Constraints on the amplitude of the NLA model as a function of redshift. The points are color-coded according to the mean sample luminosity, and different symbols are assigned to different survey samples (see Table 1). The dashed lines are the best-fitting model prediction at $z = 0.54$ obtained by Joachimi et al. (2011; Equation (7)) for $\langle M_r \rangle = -21.45$ (green) and -20.35 (blue).
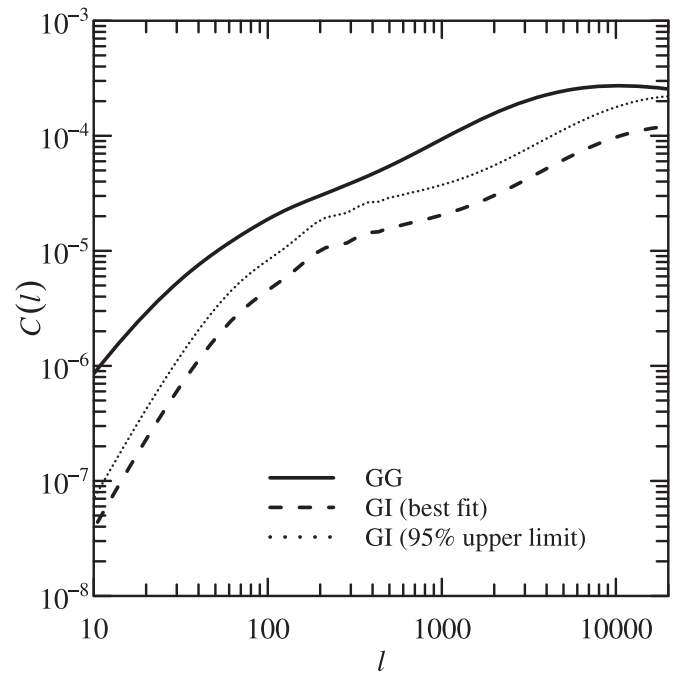

Figure 3. Forecast of the angular power spectrum of GG (solid) and GI (lower dashed) terms. The redshift distribution of the shape sample is used to compute them. The GI power spectrum is based on the best-fitting NLA model. The maximum contribution of the GI spectrum within the 95% confidence level is shown as the dotted line.

such as the stellar mass and galaxy bias may be preferable. Of course, the redshift dependence of A^{LA} could be purely physical; galaxy/halo interactions such as mergers can reduce IAs toward $z = 0$, as seen in N-body simulations (Kurita et al. 2021). Obtaining data points at different redshifts (e.g., $z \sim 0.8$) is desirable to explore this possibility.

4.4. Contaminantion to Weak Lensing Measurements

Finally, we examine how the measured GI at $z \sim 1.3$ could contaminate weak lensing signals. Figure 3 presents the comparison between the expected weak-lensing power spectrum (C_{GG}) and two predictions of contamination from the IA (C_{GI}), one being the 2σ upper limit ($A^{\mathrm{LA}} \sim 50$) and the other the best-fitting model ($A^{\mathrm{LA}} \sim 25$). We use the redshift distribution of the CFHTLenS sample to compute the angular power spectra. The contamination estimated from the best-fitting LA model is $C_{\mathrm{GI}}/C_{\mathrm{GG}} = 23\%$ (26%) at $l = 100$ (5000). We follow the procedure carried out by Tonegawa et al. (2018) to infer the resulting systematic error on Ω_m and σ_8 and find $\Delta\sigma_8 = -0.076$ and $\Delta\Omega_m = -0.054$ for $A^{\mathrm{LA}} = 27.48$ when $100 < l < 5000$ is used. At $z > 1$, the fraction of late-type galaxies that have much weaker IA increases, and thus the actual contamination will be smaller. Nevertheless, since upcoming lensing surveys aim at subpercent precision, the effect of IA should be taken into account properly.

5. Conclusions

We have reported the first possible evidence for IA of elliptical galaxies at $z > 1$ using the CFHTLenS and FastSound survey data. The GI cross correlation function between galaxy positions and shapes yielded 2.4σ level signals for the red galaxies. The constraint on the amplitude IA for red galaxies, $27.48^{+11.53}_{-11.54}$, was larger than the value extrapolated from the low-redshift measurements. Ongoing and future galaxy surveys will greatly improve the precision at such high redshifts, providing more information on the evolution of the IA. By performing the Fisher matrix analysis, we reconfirmed at $z \sim 1.3$, that future lensing surveys would require the mitigation of IAs to deliver their best performances in giving accurate cosmological implications.

We did not find any signal of GI for blue galaxies, consistent with earlier studies (Mandelbaum et al. 2011; Tonegawa et al. 2018), while upcoming galaxy surveys such as the Subaru Prime Focus Spectrograph (Takada et al. 2014) target blue galaxies at high redshifts. Recently, an interesting work of Shi et al. (2021) presented a method to quantify IA of blue galaxies. Thus, not only red galaxies but blue galaxies can be good tracers of the tidal field. Our analysis provides the first step in utilizing IA measurements in future surveys as a powerful probe of cosmology.

Appendix A
Systematics Tests

In this Appendix, we provide some tests to ensure that our estimate of the GI correlation is not affected by systematic effects. First, we present the measurements of w_{g+} using two estimators, Equations (1) and (3). The solid red and dashed blue lines of Figure 4 compare w_{g+} from the two estimators, respectively. There is a negligibly small difference, confirming that our result is unchanged by choice of the estimators.

Another test involves the shuffling of ellipticity values in the shape sample. After the randomization, the shape should no longer correlate with the density field, and w_{g+} is expected to be zero. We show the result in Figure 4 as the dotted red line. It is indeed consistent with zero at $\bar{r}_p > 3$ Mpc h^{-1}, where we assumed that our data are free from the systematics, indicating that our observed GI signal manifests the true intrinsic shear-density correlation.
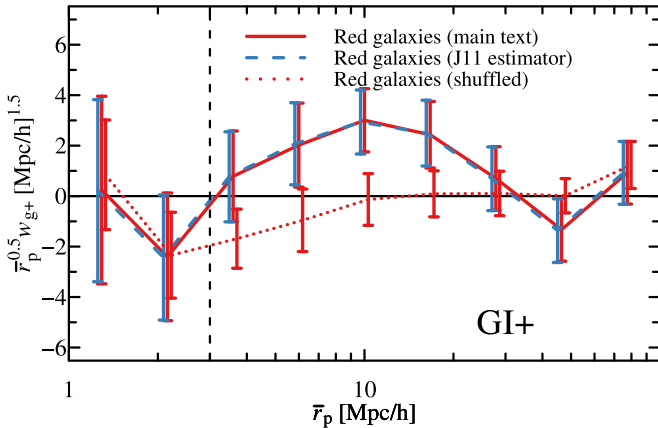
Figure 4. Projected correlation functions $w_{g+}(\bar{r}_p)$ measured with different settings as a diagnosis for systematics. The solid red line is identical to that in Figure 1. The dashed blue line is obtained by using the estimator (3). The dotted red line is the same as the solid red line except that the ellipticity of the shape sample is shuffled.

Appendix B
Theoretical Modeling of Correlation Functions

In this Appendix, following Joachimi et al. (2011), we summarize the modeling of the correlation function, including photo-z uncertainties (Appendix B.1) and contributions of gravitational lensing under the Limber approximation (Appendix B.2).

B.1. The Effect of Photo-z Uncertainties

If we denote quantities determined via photo-z by a bar, the GI correlation function measured in a photo-z survey is expressed by an integral of the true one, $\xi_{g+}^{\rm spec}$, as

$$\xi_{\rm gI}(\bar{r}_p, \bar{r}_\pi, \bar{z}_{\rm m}) = \int dz_{\rm m} \int dr_p$$
$$\times \int dr_\pi p(r_p, r_\pi, z_m | \bar{r}_p, \bar{r}_\pi, \bar{z}_m) \xi_{\rm gI}^{\rm spec}(r_p, r_\pi, z_{\rm m}), \quad (B1)$$

where $p(r_p, r_\pi, z_m | \bar{r}_p, \bar{r}_\pi, \bar{z}_m)$ is the conditional probability distribution of (r_p, r_π, z_m) for given $(\bar{r}_p, \bar{r}_\pi, \bar{z}_m)$ and z_m is the mean redshift of the density (z_1) and shape (z_2) samples, $z_{\rm m} = \frac{1}{2}(z_1 + z_2)$. We use the approximation for the pair separations (r_p, r_π), as $r_p \approx \theta \chi(z_{\rm m})$ and $r_\pi \approx (c/H(z_{\rm m}))(z_2 - z_1)$, and change the variables from (r_p, r_π) to (z_1, z_2). We then obtain the expression,

$$\xi_{\rm gI}(\bar{r}_p, \bar{r}_\pi, \bar{z}_{\rm m}) = \int dz_1 \int dz_2 p_n(z_1|\bar{z}_1) p_\epsilon$$
$$\times (z_2|\bar{z}_2) \xi_{\rm gI}^{\rm spec}\left(\bar{r}_p \frac{\chi(z_{\rm m})}{\chi(\bar{z}_{\rm m})}, \frac{c(z_2 - z_1)}{H(z_{\rm m})}, z_{\rm m}\right), \quad (B2)$$

where $z_{\rm m}$ is given above and $\bar{z}_{1,2} = \bar{z}_{\rm m} \mp \bar{r}_\pi H(\bar{z}_{\rm m})/2c$. To obtain Equation (B2), we have assumed that photo-z affects only the radial distances but not the angular positions. The factor $\chi(z_{\rm m}))/\chi(\bar{z}_{\rm m})$ arises from the assumption that θ is conserved. In our analysis, the density sample has spectroscopic redshifts. Thus setting $p_n(z_1|\bar{z}_1) = \delta^{\rm D}(z_1 - \bar{z}_1)$ leads to Equation (6).

B.2. Limber Approximations

The cross correlation of galaxy position and ellipticity, denoted as the $n\epsilon$ term, contains contributions not only from the gI correlation but also from galaxy–galaxy lensing (gG), magnification-shear correlations (mG), and magnification-intrinsic ellipticity correlations (mI). In terms of projected angular power spectra including the photo-z's, $\bar{z}_1$ and $\bar{z}_2$, we can write it as

$$C_{n\epsilon}(\ell; \bar{z}_1, \bar{z}_2) = C_{\rm gI}(\ell; \bar{z}_1, \bar{z}_2) + C_{\rm gG}(\ell; \bar{z}_1, \bar{z}_2)$$
$$+ C_{\rm mG}(\ell; \bar{z}_1, \bar{z}_2) + C_{\rm mI}(\ell; \bar{z}_1, \bar{z}_2). \quad (B3)$$

Under the Limber approximations, these angular power spectra are given by (e.g., Joachimi & Bridle 2010),

$$C_{\rm gI}(\ell; \bar{z}_1, \bar{z}_2) = b_g \int_0^{\chi_{\rm hor}} d\chi' \frac{p_n(\chi'|\chi(\bar{z}_1)) p_\epsilon(\chi'|\chi(\bar{z}_2))}{\chi'^2}$$
$$\times P_{\delta\rm I}\left(\frac{\ell}{\chi'}, z(\chi')\right), \quad (B4)$$

$$C_{\mathrm{gG}}(\ell;\,\bar{z}_1,\,\bar{z}_2) = b_g \int_0^{\chi_{\mathrm{hor}}} d\chi' \frac{p_n(\chi'|\chi(\bar{z}_1)) q_\epsilon(\chi',\,\chi(\bar{z}_2))}{\chi'^2}$$
$$\times P_\delta\left(\frac{\ell}{\chi'},\,z(\chi')\right),$$

$$C_{\mathrm{mG}}(\ell;\,\bar{z}_1,\,\bar{z}_2) = 2(\alpha_s - 1)$$
$$\times \int_0^{\chi_{\mathrm{hor}}} d\chi' \frac{q_n(\chi',\,\chi(\bar{z}_1)) q_\epsilon(\chi',\,\chi(\bar{z}_2))}{\chi'^2}$$
$$\times P_\delta\left(\frac{\ell}{\chi'},\,z(\chi')\right),$$

(B5)

$$C_{\mathrm{mI}}(\ell;\,\bar{z}_1,\,\bar{z}_2) = 2(\alpha_s - 1)$$
$$\times \int_0^{\chi_{\mathrm{hor}}} d\chi' \frac{q_n(\chi',\,\chi(\bar{z}_1)) p_\epsilon(\chi'|\chi(\bar{z}_2))}{\chi'^2}$$
$$\times P_{\delta\mathrm{I}}\left(\frac{\ell}{\chi'},\,z(\chi')\right),$$

(B6)

where χ_{hor} is the comoving horizon distance, α_s is the logarithmic slope of the cumulative galaxy luminosity function of the density sample, and q_x ($x = \{n,\,\epsilon\}$) is the lensing weight function,

$$q_x(\chi,\,\chi_1) = \frac{3H_0^2\Omega_m}{2c^2} \frac{\chi}{a(\chi)} \int_\chi^{\chi_{\mathrm{hor}}} d\chi' p_x(\chi'|\chi_1) \frac{\chi' - \chi}{\chi'}. \quad (B7)$$

Using these angular power spectra, the three-dimensional correlation functions are obtained as

$$\xi_X(\bar{r}_p,\,\bar{r}_\pi;\,\bar{z}_{\mathrm{m}}) = -\int_0^\infty \frac{d\ell}{2\pi} \ell J_2(\ell\theta(\bar{r}_p,\,\bar{z}_{\mathrm{m}}))$$
$$\times C_X(\ell;\,\bar{z}_1(\bar{z}_{\mathrm{m}},\,\bar{r}_\pi),\,\bar{z}_2(\bar{z}_{\mathrm{m}},\,\bar{r}_\pi)), \quad (B8)$$

where $X = \{\mathrm{gI,\,gG,\,mG,\,mI}\}$. By comparing ξ_{gI} obtained in this way to the full expression, Equation (B2), we have verified that the Limber approximation is accurate enough within the measurement uncertainties.

ORCID iDs

Teppei Okumura ⬤ https://orcid.org/0000-0002-8942-9772

References

Benítez, N. 2000, ApJ, 536, 571
Blazek, J., McQuinn, M., & Seljak, U. 2011, JCAP, 5, 10
Bridle, S., & King, L. 2007, NJPh, 9, 444
Capak, P. L. 2004, PhD thesis, University of Hawai'i
Catelan, P., Kamionkowski, M., & Blandford, R. D. 2001, MNRAS, 320, L7
Chisari, N., Laigle, C., Codis, S., et al. 2016, MNRAS, 461, 2702
Chisari, N. E., & Dvorkin, C. 2013, JCAP, 12, 029
Coleman, G. D., Wu, C. C., & Weedman, D. W. 1980, ApJS, 43, 393
Croft, R. A. C., & Metzler, C. A. 2000, ApJ, 545, 561
Du, W., Cheng, C., Zheng, Z., & Wu, H. 2020, AJ, 159, 138
Erben, T., Hildebrandt, H., Miller, L., et al. 2013, MNRAS, 433, 2545
Fioc, M., & Rocca-Volmerange, B. 1999, arXiv:astro-ph/9912179
Hamilton, A. J. S. 1993, ApJ, 417, 19
Hamilton, A. J. S. 1998, in Astrophysics and space science library, The evolving universe, Selected topics on large-scale structure and on the properties of galaxies 231 ed. D. Hamilton (Dordrecht: Kluwer), 185
Heavens, A., Refregier, A., & Heymans, C. 2000, MNRAS, 319, 649
Hildebrandt, H., Erben, T., Kuijken, K., et al. 2012, MNRAS, 421, 2355
Hirata, C. M., Mandelbaum, R., Ishak, M., et al. 2007, MNRAS, 381, 1197
Hirata, C. M., & Seljak, U. 2004, PhRvD, 70, 063526
Hirata, C. M., & Seljak, U. 2010, PhRvD, 82, 049901
Iwamuro, F., Moritani, Y., Yabe, K., et al. 2012, PASJ, 64, 59
Joachimi, B., & Bridle, S. L. 2010, A&A, 523, A1
Joachimi, B., Cacciato, M., Kitching, T. D., et al. 2015, SSRv, 193, 1
Joachimi, B., Mandelbaum, R., Abdalla, F. B., & Bridle, S. L. 2011, A&A, 527, A26
Johnston, H., Georgiou, C., Joachimi, B., et al. 2019, A&A, 624, A30
Johnston, H., Joachimi, B., Norberg, P., et al. 2021, A&A, 646, A147
Kirk, D., Brown, M. L., Hoekstra, H., et al. 2015, SSRv, 193, 139
Kurita, T., Takada, M., Nishimichi, T., et al. 2021, MNRAS, 501, 833
Mahajan, S., Drinkwater, M. J., Driver, S., et al. 2018, MNRAS, 475, 788
Mandelbaum, R., Blake, C., Bridle, S., et al. 2011, MNRAS, 410, 844
Mandelbaum, R., Hirata, C. M., Ishak, M., Seljak, U., & Brinkmann, J. 2006, MNRAS, 367, 611
Miller, L., Kitching, T. D., Heymans, C., Heavens, A. F., & van Waerbeke, L. 2007, MNRAS, 382, 315
Okada, H., Totani, T., Tonegawa, M., et al. 2016, PASJ, 68, 47
Okumura, T., Hayashi, M., Chiu, I. N., et al. 2021, PASJ, 73, 1186
Okumura, T., Hikage, C., Totani, T., et al. 2016, PASJ, 68, 38
Okumura, T., & Jing, Y. P. 2009, ApJL, 694, L83
Okumura, T., Jing, Y. P., & Li, C. 2009, ApJ, 694, 214
Okumura, T., & Taruya, A. 2020, MNRAS, 493, L124
Okumura, T., Taruya, A., & Nishimichi, T. 2020, MNRAS, 494, 694
Samuroff, S., Mandelbaum, R., & Blazek, J. 2021, MNRAS, 508, 637
Scalo, J. M. 1986, FCPh, 11, 1
Schlegel, D. J., Finkbeiner, D. P., & Davis, M. 1998, ApJ, 500, 525
Shi, J., Osato, K., Kurita, T., & Takada, M. 2021, ApJ, 917, 109
Singh, S., Mandelbaum, R., & More, S. 2015, MNRAS, 450, 2195
Takada, M., Ellis, R. S., Chiba, M., et al. 2014, PASJ, 66, 1
Takahashi, R., Sato, M., Nishimichi, T., Taruya, A., & Oguri, M. 2012, ApJ, 761, 152
Taruya, A., & Okumura, T. 2020, ApJL, 891, L42
Tonegawa, M., Okumura, T., Totani, T., et al. 2018, PASJ, 70, 41
Tonegawa, M., Totani, T., Okada, H., et al. 2015, PASJ, 67, 81
Wang, W., Jing, Y. P., Li, C., Okumura, T., & Han, J. 2011, ApJ, 734, 88
Yao, J., Shan, H., Zhang, P., Kneib, J.-P., & Jullo, E. 2020, ApJ, 904, 135